Contents lists available at ScienceDirect

Ocean Engineering

Research paper

Combined CFD-EFD methods applied to determining the form factor of vessels with very low length to beam ratio ⋆

S. Oyuela [a,b], H. R. Díaz-Ojeda [c,**], A. D. Otero [a,d], R. Sosa [a,b]

[a] *Universidad de Buenos Aires (UBA), Facultad de Ingeniería, Paseo Colón 850, Buenos Aires, C1063, Argentina*
[b] *CONICET - Universidad de Buenos Aires. Laboratorio de Ingeniería Naval y Oceánica (LabHiNO), Instituto de Tecnologías y Ciencias de la Ingeniería "Hilario Fernández Long" (INTECIN), Paseo Colón 850, Buenos Aires, C1063, Argentina*
[c] *Universidad de Las Palmas de Gran Canaria, Campus de Tafira, Las Palmas de Gran Canaria, 35017, España,*
[d] *CONICET, Centro de Simulación Computacional para Aplicaciones Tecnológicas, Godoy Cruz 2390, Buenos Aires, C1425FQD, Argentina*

ARTICLE INFO

ABSTRACT

This study investigates the influence of scale effects on form factor determination for a fishing vessel with a low length-to-beam (L/B) ratio, using a combined Experimental Fluid Dynamics (EFD) and Computational Fluid Dynamics (CFD) approach. The research compares the behavior of the form factor between a fishing vessel and the well-known KCS benchmark hull. Results show that scale effects have a more significant impact on the fishing vessel, particularly due to increased viscous pressure losses in the stern region. While the non-dimensional frictional resistance component remains similar between both hulls, the non-dimensional pressure component differ significantly, highlighting the influence of hull shape on pressure recovery. The comparison with empirical methods reveals that traditional marine formulations may not adequately capture full scale form factor of hulls with very low length to beam ratio. Instead, the form factor obtained using aircraft drag estimation approaches shows better agreement with CFD predictions at full scale. Based on these findings, the adoption of distinct form factor values at model and full scale is recommended for vessels with similar geometric characteristics, in contrast to conventional extrapolation practices that assume a constant form factor. This methodology may improve the accuracy of effective power predictions and support more reliable design evaluations.

1. Introduction

In the field of ship hydrodynamics, a significant concern pertains to the extrapolation of total force from model tests to real-scale ships since it is vital for the engine selection among other decisions. In this context, the form factor is a critical parameter that represents the additional resistance caused by the hull's shape compared to a flat plate. Accurate determination of the form factor is essential for predicting ship resistance, power requirements, and energy efficiency at real scale.

Hughes (Hughes, 1954) introduced the concept of form factor (k), proposing that viscous ship resistance can be decomposed into frictional resistance (proportional to a flat plate) and form resistance (due to the hull's shape). This concept underlies contemporary form factor determination methods, including the Prohaska method, widely used for experimental extrapolation, as well as CFD-based approaches.

Traditionally, k has been determined through experimental fluid dynamics (EFD) techniques, with the Prohaska method being the standard recommended by the International Towing Tank Conference (ITTC) (Committee, 2011). It estimates the form factor by extrapolating low-speed resistance data. While generally regarded as the most reliable method based on model testing, it presents several well-documented limitations, which can be grouped into three main categories: the assumption of linearity between resistance components, experimental uncertainties, and scale effects.

The Prohaska method assumes a linear relationship between resistance components, which breaks down for hulls with pronounced bulbous bows or non-conventional shapes. These hulls generate non-linear wave-making resistance and flow separation, which lead to inaccurate form factor estimates, as shown by Korkmaz et al. (2021) and Terziev et al. (2021).

** Principal corresponding author.
E-mail addresses: soyuela@fi.uba.ar (S. Oyuela), hectorruben.diaz@ulpgc.es (H.R. Díaz-Ojeda), aotero@fi.uba.ar (A.D. Otero), rsosa@fi.uba.ar (R. Sosa).

It also amplifies experimental uncertainties, especially in partial loading conditions (e.g., ballast), where resistance measurements at low speeds are less reliable, as reported by Korkmaz et al. (2021).

The above mentioned method does not adequately account for scale effects, leading to discrepancies between model-scale and full-scale predictions. Traditionally, it has been assumed that the form factor is independent of the ship's speed (Froude number, Fn) and the Reynolds number (Rn). However, recent studies have shown that this assumption does not hold, particularly when scale effects are considered.

The dependence of the form factor on the Rn has been extensively studied, both experimentally and computationally. It has been observed that the form factor varies with Rn due to changes in the boundary layer thickness and pressure distribution around the hull. García-Gómez (García-Gómez, 2000) and Terziev et al. (2019) demonstrated that the form factor depends on the Rn. At low Rn (model scale), the form factor changes more rapidly than at high Rn (full scale). This is because the boundary layer is thicker at small scales, which affects the form resistance.

WANG et al. (2015) proposed numerical friction lines derived from CFD simulations of flat plates, offering an alternative to the ITTC-57 correlation line. Their work demonstrated that using numerical friction lines reduces the speed dependency of the form factor, a finding corroborated by Korkmaz et al. (2021).

The dependence of the form factor on Fn has been less studied but is also the subject of recent research. The Fn influences wave-making resistance and the ship's sinkage and trim, which in turn can affect the form resistance. Sinkage and trim change with Fn, affecting the wetted surface area and pressure distribution around the hull. This can influence the form factor. For example,(Yokoo, 1960) proposed corrections for the form factor based on changes in sinkage and trim, although these corrections have not been widely validated.

(2021) (Terziev et al., 2021) conducted double-body simulations to isolate the effect of Fn on the form factor, using CFD simulations to analyze k at different scales and speeds. Their study found that the k is highly sensitive to the turbulence model used, especially at low speeds (low Fn). However, at higher speeds ($Fn > 0.15$), the dependence of k on Fn becomes negligible.

A thorough examination of the impact of scale effects on ship hydrodynamics in general, and on the form factor in particular, can be found in Terziev et al. (2022).

The limitations of the EFD methods have motivated the development of alternative approaches, particularly those based on CFD, which can provide a more detailed and accurate decomposition of resistance components. CFD has also gained prominence for its ability to satisfy both Fn and Rn similarity. Over the past few decades, the use of CFD methods based on the Navier-Stokes equations has increased dramatically (Larsson et al., 2013, 2010). This development has facilitated the enhancement of techniques and procedures for the precise prediction of ship resistance on a model scale. Nevertheless, concerns persist regarding the reliability of CFD in predicting the performance of full-scale vessels (Terziev et al., 2022).

Combined CFD-EFD methods have emerged as a promising alternative, leveraging the strengths of both numerical simulations and experimental data to improve the accuracy and robustness of form factor predictions. Combined CFD-EFD methods aim to integrate the strengths of numerical simulations and experimental testing. CFD provides a detailed description of the flow around the hull, enabling precise decomposition of resistance into frictional and pressure components, and EFD offers experimental data for validation and calibration of CFD models, ensuring their reliability.

As the form factor is marked as one of the major points of uncertainty when extrapolating results by the ITTC specialist committee of CFD-EFD combined methods (Committee, 2021), Korkmaz et al. (2021) proposed a CFD-based form factor determination method, replacing the Prohaska method with double-body (DB) Reynolds Average Navier-Stokes (RANS) simulations. The authors found that the CFD-based form factor predictions showed good agreement with experimental results for the KVLCC2 and KCS hulls, particularly in design loading conditions. The CFD method demonstrated lower scatter in form factor predictions compared to the Prohaska method, suggesting greater robustness. The study confirmed that k depends on Rn, highlighting the importance of accounting for scale effects in resistance predictions.

In this context, the proposed study is to ascertain the form factor determination by CFD DB for a fishing vessel, and the potential for enhancing performance prediction through the utilization of combined CFD-EFD methodologies. Fishing vessels with a relatively short length (LWL < 35 m) and a low length/breadth (L/B < 4) were selected for this research.

It is worth noting that most of the studies of CFD-EFD combined methods have been conducted on benchmark vessels, and there is limited or no literature available on other types of ships, such as fishing vessels.

We have recently validated a numerical model to study the flow around a 1:20 scale physical model of a fishing vessel (Oyuela et al., 2024). This model was able to adequately reproduce the total resistance values and the wave pattern of the physical model moving in calm water. In that work, the k values obtained with EFD measurements (using the Prohaska method) were compared with k values obtained by CFD using DB. While the CFD values exhibited a considerably lower uncertainty compared to the EFD values, it was observed that employing two distinct Fn values for the DB CFD model resulted in substantially different k values.

At this juncture in the investigation, a number of issues have been identified that necessitate further consideration with regard to the relationship between k and the model speed.

1. Is it possible that our implementation of the CFD double-body (DB) model is incorrect, leading to an artificial or spurious dependence in the results?
2. Is this dependence on model velocity caused by a variation of Fn or the Rn?
3. Is this dependence a characteristic specific to this type of vessel, or has a similar dependence been observed in other vessel types?
4. Regarding the extrapolation process, if such a dependence is confirmed, what value of the form factor should be adopted?

In the present work, the k results (both numerical and experimental) of the fishing vessel are compared with those of the reference vessel KCS in order to answer these questions.

A physical model of the KCS has been constructed at the LabHiNO (Laboratorio de Hidrodinámica Naval y Oceánica, Laboratory of Naval and Ocean Hydrodynamics) at 1:79 scale for the purpose of conducting EFD tests and determining k by means of the Prohaska method. In addition, a numerical model of the KCS at 1:79 scale has been developed to obtain k using the CFD DB method.

The KCS vessel was selected for this study due to its extensive research history and the potential for two key insights. Firstly, the validation of the CFD DB model. Secondly, the discrimination of whether the observed behavior is indicative of the studied vessel type or a more general phenomenon.

To perform a more detailed analysis of the dependence of k on Rn, the CFD DB calculations of k have been extended to larger scales than that of the physical model for the fishing vessel.

The structure of the paper is as follows. The "Experimental and numerical setup" section details the vessels that were studied, the characteristics of the physical tests, and the specifications of the CFD models for the numerical tests of both vessels. The "Result" section begins with the presentation of the values of k obtained by the Prohaska method and the CFD DB method for the KCS, followed by a comparison of these values with those documented in the literature. Subsequently, the values of k for the fishing vessel are exhibited, in conjunction with a comparison of these values with those obtained for the KCS.

Table 1
Main dimensions of the full scale KCS and its scaled model.

Parameter (Symbol)	Unit	Full scale	Model (1:79)
Model scale (λ)	–	1	79
Length (L)	m	230.000	2.911
Breadth (B)	m	32.200	0.407
Draught (T)	m	19.000	0.240
Displacement (vol.) (∇)	m³	52,030	0.106
Displacement (mass)	ton	53377.577	0.105
Reynolds Number (Rn)[a]	–	$2.69e+09$	$3.84e+06$

[a] Corresponds to design speed at $Fn = 0.26$.

In the "Analysis" section, an examination of the form factor behavior of the fishing vessel with respect to Rn will be conducted. The analysis will consider the various aspects that could influence it. Firstly, the effect of the frictional line will be discussed. Then, the force decomposition, the pressure distribution on the hull, and the effect of the L/B ratio will be presented. Finally, comments and conclusions will be made regarding the effect of the value of k on total resistance and effective power predictions.

2. Experimental and numerical setup

In this section, a description of the different hull's characteristics used for the research are introduced as well as the numerical and experimental procedure. Additionally, a description of the experimental facilities employed and CFD code will be included.

2.1. Physical vessel models

For the purpose of this work a fishing vessel and a container ship (KCS) were selected. They were constructed following the procedure recommended by the ITTC (Specialist Committee: Procedures for Resistance and Propeller Open Water Tests of 23rd ITTC, 2002). Both hulls were built using glass fiber-reinforced plastic (GFRP) to ensure structural integrity and surface smoothness. To induce turbulence, two 1.0 mm diameter tripwires were applied. One was positioned aft of the forward perpendicular at a distance equivalent to 5% of L_{WL}, while the other was placed behind the leading edge of the bulb, at a distance corresponding to one-third of the bulb's length.

The KRISO Container Ship (KCS) is a well-known benchmark hull form used in a large variety of hydrodynamic research, validation and verification of CFD simulations. Developed by the Korea Research Institute of Ships and Ocean Engineering (KRISO), it represents a modern container ship with a bulbous bow, a transom stern, and a characteristic hull shape optimized for resistance and propulsion studies. The KCS has been extensively tested in towing tanks and numerical simulations, making it a standard reference for ship hydrodynamics research.

Due to the dimensions of the towing tank and to avoid blockage effects, the adopted scale was 1:79. Main dimensions are presented in Table 1. Fig. 1 shows a side and isometric view of the fabricated model.

The KCS model was used to verify and validate the accuracy of both the experimental and numerical setups against previous literature. Following this verification, a fishing vessel with a low L/B ratio was analyzed as the primary focus of the study. The fishing vessel model was constructed at a scale of $\lambda = 20$, following the same ITTC-recommended construction methodology applied to the KCS model.

Table 2 presents the principal characteristics of both the full-scale fishing vessel and its model.

Although in the work of Oyuela et al. (2024) we have studied three different loading conditions (i.e. ballast, intermediate and full loading), the present study has concentrated on the examination of the full loading condition. The results presented in this work concerning the full load condition have been found for the other two conditions. However, for the sake of simplicity, it has been decided to show the results for only

(a) Side view.
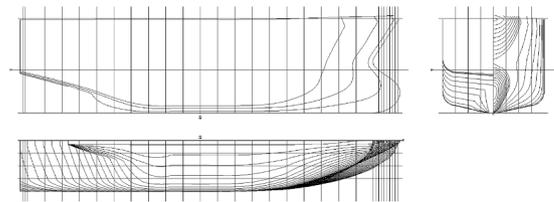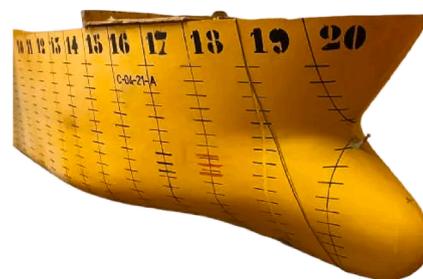

(b) Perspective view.

Fig. 1. KCS model scale (1:79).

Fig. 2. Fishing vessel body lines plan.

(a) Side view.

(b) Perspective view.

Fig. 3. Fishing vessel model (1:20).

one loading condition. Fig. 2 illustrates the hull's body lines and Fig. 3 shows a side and perspective view of the fabricated model.

Table 3, from Yılmaz and Kükner (1999), presents various series of fishing vessels and the one of the present study, demonstrating that the analyzed model falls within the L/B ratios of several widely used series. This context underscores the significance of studying the scale effects on form factor, as such analysis can have a substantial impact on understanding the hydrodynamic behavior of vessels with low aspect ratios.

Table 2

Main dimensions of the full scale fishing vessel and its scaled model.

Parameter (Symbol)	Unit	Full scale	Model (1:20)
Model scale (λ)	–	1	20
Length WL (L_{WL})	m	32.680	1.641
Length OS (L_{OS})	m	34.795	1.670
Breath (B)	m	9.280	0.464
Draught (T)	m	3.300	0.195
Disp. vol. (∇)	m^3	599.400	0.095
Wetted area (S)	m^2	392.670	1.124
Block coeff. (C_B)	–	0.600	0.600
Midship coeff. (C_M)	–	0.860	0.890
Reynolds Number (Rn)[a]	–	$1.43e+08$	$1.60e+06$

[a] Corresponds to design speed at $Fn = 0.25$.

Table 3

Parameters intervals for classic fishing vessel series and the present study fishing vessel (FV).

Series	L_{WL}/B_{WL}	B_{WL}/T	C_B	$L_{WL}/\nabla^{1/3}$
UBC	2.60-4.00	2.00–3.00	0.53-0.61	3.00–4.47
ITU	3.30-5.00	2.00–3.20	0.35-0.56	3.40-6-10
BSRA	4.30-5.80	2.00–3.00	0.53-0.63	4.35-5.10
Ridgely-N.	3.20-5-75	2.30	0.42-0.53	3.85-5.22
Model				
FV	3.53	2.38	0.64	3.59

2.2. Experimental facility

The resistance tests were conducted in the towing tank of Laboratory of Naval and Ocean Hydrodynamics (LabHiNO, Laboratorio de Hidrodinámica Naval y Oceánica) at the University of Buenos Aires (UBA), Argentina. For the tests, the models were carefully ballasted to match the target displacements and waterlines before being mounted on a Kempf & Remmers R 47 single-component load cell. The connection between the trolley and the load cell was configured to constrain all degrees of freedom except heave, and pitch, thereby permitting the model to freely adjust its trim and sinkage. The resistance transducer, designed to handle loads up to ± 100 N, had a sensitivity of approximately ± 1 mV/V of supply voltage. Regarding the mean cross-sectional area of the models, it represented 1.2% of the cross section of the towing tank for the fishing vessel and 1.4% for the KCS. To compensate for blockage effects, where necessary, Schuster's blockage correction method was applied following the ITTC guidelines.

The experimental setup and uncertainty analysis for the fishing vessel model were previously described in Oyuela et al. (2024). The tests were conducted following ITTC recommendations (Committee, 2011), resulting in an estimated uncertainty in resistance measurements between 0.83% and 1.38% at $0.1 < Fn < 0.37$ for the fishing vessel. For the KCS model, uncertainty 0.02% and 1.86% at $0.02 < Fn < 0.40$ was reached.

2.3. Resistance tests uncertainty analysis

The uncertainty analysis of the resistance tests was carried out following the ITTC recommended procedures (Group, 2017). The methodology accounts for the main sources of uncertainty involved in the measurement of total resistance, including contributions from hull geometry, towing speed, water temperature, dynamometer calibration and replicate testing. These components are estimated separately and subsequently combined through the Root Sum Square (RSS) method to obtain the overall standard uncertainty. A detailed description of the adopted methodology and its application to the fishing vessel model is available in Oyuela et al. (2024).

For the present work, the same uncertainty-assessment procedure was applied to both the fishing vessel and the KCS model. For the fishing vessel, the uncertainty in the measured total resistance varies with the Froude number, showing very low values across most of the tested range. Specifically, the expanded uncertainty decreases to below 0.2% for $0.10 \leq Fn \leq 0.30$, with representative values such as 0.028% at $Fn = 0.10$, 0.112% at $Fn = 0.16$, and 0.009% at $Fn = 0.20$. The highest uncertainties occur at the upper end of the tested range, reaching 1.382% at $Fn = 0.36$ and 13.433% at $Fn = 0.40$. Despite these two outliers, the overall uncertainty level remains low throughout the operating range relevant for form-factor determination.

For the KCS model, the uncertainty levels were considerably lower due to the higher model scale and dynamometer sensitivity, ranging from 1.86% at $Fn = 0.02$ to 0.02% at $Fn = 0.40$. The expanded uncertainties correspond to a 95% confidence level.

Overall, the dominant sources of uncertainty were associated with the calibration of the dynamometer and the variability among repeated tests at low speeds. At higher speeds, the relative contribution of these components diminishes, resulting in lower overall uncertainty levels. These results ensure the reliability of the resistance measurements used in the present study.

2.4. Numerical vessel models

2.4.1. Numerical methods

This section describes the numerical set-up used for all the simulations. The open-source finite volume code OpenFOAM 11 was employed. This study builds upon the findings presented in Oyuela et al. (2024), where a detailed account of the numerical settings can be found.

To model turbulence, Reynolds Averaged Navier Stokes (RANS) simulations were selected, with the PIMPLE algorithm to handle pressure-velocity coupling, providing a robust approach suitable for transient simulations with large Courant numbers. The localEuler scheme was used for time advancement. Convergence was assessed by monitoring the force oscillations, ensuring they remained below 1% before terminating each simulation.

Regarding turbulence modeling, among all the turbulence models studied by Terziev et al. (2021) or Pena and Huang (2021), the k-ω SST turbulence model was used in the present work due to its well-established balance between accuracy and robustness, particularly in near-wall regions and adverse pressure gradients.

2.4.2. Numerical domain and boundary conditions

The computational domain presented in Fig. 4 followed the ITTC guidelines (Comittee, 2017), maintaining the same spatial configuration for both the fishing vessel and the KCS model. The inlet was positioned 1.5 ship lengths upstream of the forward perpendicular, where a uniform velocity condition was applied. The outlet was placed 2.5 ship lengths downstream of the aft perpendicular, with a zero-gradient condition for all variables. Side and bottom boundaries were set 2.5 ship lengths away from the hull centerline to minimize blockage effects. A symmetry condition was imposed on these boundaries. At the top boundary a symmetry condition was used at the draught plane, since only double body, single phased simulations were run. The ship hull was assigned a no-slip wall condition, with the near-wall region modeled using the `kLowReWallFunction` available in OpenFOAM. This treatment adapts to the local value of y^+, providing a consistent representation of the boundary layer across different Froude numbers without requiring strict constraints on y^+. In almost all cases, the monitored distribution showed average values below $y^+ \approx 300$, which lies within recommended limits reported in previous studies (Pena and Huang, 2021; Korkmaz et al., 2021), ensuring adequate near-wall resolution and reliable predictions for the scale effect analysis.

Although the numerical setup adopts a double-body approximation, thereby neglecting free-surface effects, this choice remains consistent with the objectives of the present study. In the experiments, the form
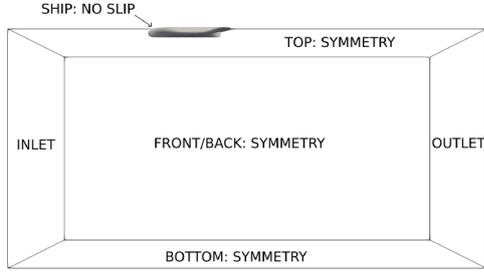
Fig. 4. Numerical domain.

factor was determined using the Prohaska method, which relies on resistance tests at very low Froude numbers in order to minimize wave-making contributions. Under such conditions, the measured resistance is predominantly viscous, and the influence of the free surface is negligible. Consequently, the double-body CFD approach provides a valid counterpart for comparison with the experimental results. Thus, despite the different boundary conditions between the free-surface EFD tests and the double-body CFD simulations, the methodology is coherent and appropriate for the determination of the form factor.

2.4.3. Mesh convergence

To ensure the reliability of the numerical results, a grid convergence study was conducted following the guidelines proposed by Freitas et. al (Freitas, 2020), as well as the recommendations from the ITTC (Comittee, 2017) and ASME (American Society of Mechanical Engineers, 2009). The Grid Convergence Index (GCI) method was applied to quantify discretization errors and assess whether the solution exhibits monotonic or oscillatory convergence.

The GCI is based on the Richardson extrapolation approach and provides a measure of how the numerical solution approaches the asymptotic grid-independent value. The study was performed using three systematically refined grids: coarse, medium, and fine, with a refinement factor r between successive grids, defined as:

$$r = \frac{h_{coarse}}{h_{medium}} = \frac{h_{medium}}{h_{fine}} \qquad (1)$$

where h represents the characteristic grid size, typically calculated as:

$$h = \left(\frac{1}{N}\sum_{i=1}^{N} V_i\right)^{1/3} \qquad (2)$$

where V_i is the volume of the i-th control cell, and N is the total number of cells in the computational domain.

The apparent order of accuracy p was determined using the following expression:

$$p = \frac{ln\left(\frac{\epsilon_{medium,fine}}{\epsilon_{coarse,medium}}\right)}{ln(r)} \qquad (3)$$

where ϵ represents the relative difference in the numerical solution between two successive grids:

$$\epsilon_{ij} = \Phi_i - \Phi_j \qquad (4)$$

with Φ being the variable of interest, such as total resistance or pressure forces. Once three solutions are obtained, R can be calculated:

$$R = \frac{\epsilon_{21}}{\epsilon_{32}} \qquad (5)$$

Following ITTC (2008) (Comittee, 2017), the convergence behavior was categorized as:

- Monotonic convergence, when $0 < R < 1$
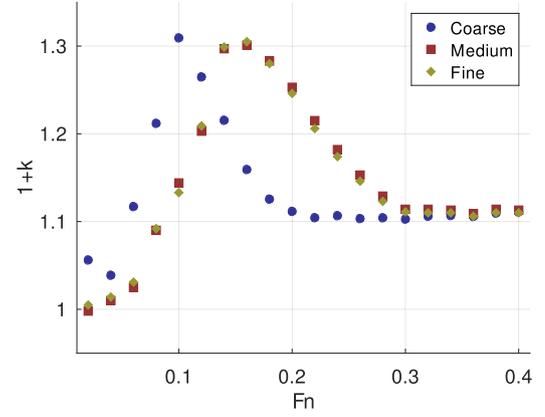- Oscillatory convergence, when $R < 0$
- Divergence, when $R > 1$

Fig. 5. Numerical $1 + k$ vs Fn for the KCS and considering three different meshes.

The GCI for the finest grid level was then computed as:

$$GCI = F \frac{\left|\frac{\Phi_1 - \Phi_2}{\Phi_1}\right|}{(r_{21}^p - 1)} \qquad (6)$$

where F = 1.25 is a safety factor recommended by ASME.

In all KCS cases, all individual simulations exhibit stable iterative behaviour with no significant force oscillations. The GCI obtained is less than 0.35% except for Fn between 0.36 and 0.40, where the GCI reaches values between 1.06% and 1.86%. Most of the cases resulted in oscillating convergence, except for Fn between 0.10 and 0.16 where monotonic convergence was reached. All of this for $r = \sqrt{2}$, resulting in mesh sizes of 633,938, 903,744 and 1,213,419 cells for *Coarse*, *Medium* and *Fine* meshes respectively. For 1:1 scale simulations, "Fine" mesh was scaled from the original 1:20 and refined till it reached 3.145.961 cells. Fig. 5 shows how *Medium* and *Fine* meshes gave almost identical results; it is for this reason that the fine mesh is used for all simulations. In cases where oscillatory behavior was observed, two additional meshes (one coarser than the *Coarse* and one finer than the *Fine*) were also tested, following the recommendation of Freitas (2020). This procedure confirmed that the oscillations correspond to convergent behavior rather than divergence, ensuring the reliability of the mesh refinement analysis.

3. Results

3.1. KCS form factor

3.1.1. Experimental form factor determination

The ITTC method of dividing the total drag coefficient (C_T) incorporates the Hughes' hypothesis (Hughes, 1954) and introduces the form factor k to augment the flat plate drag coefficient by capturing three-dimensional hull form effects. Therefore, it is possible to divide (C_T) into the following constituent parts:

$$C_T = (1 + k)C_{F0} + C_W \qquad (7)$$

where, $(1 + k)C_{F0}$ denotes the viscous resistance coefficient (C_V) and C_W represents the wave resistance coefficient. The C_V is composed of the flat plate drag coefficient (C_{F0}) and the hull shape effects on the boundary layer itself accounted as a fraction of C_{F0} by the form factor k (Comittee, 2011).

Prohaska (Prohaska, 1966) proposed a method for determining the form factor from model tests which is considered to be the most reliable method available and the one recommended by the ITTC (Comittee, 2011). It assumes that for $Fn < 0.2$, C_W can be approximated by αFn^4. So, Eq. (7) for the model can be rewritten as:

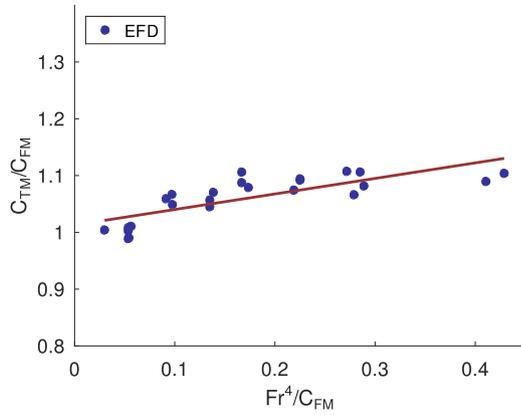$$\frac{C_{TM}}{C_{FM0}} = (1 + k) + \alpha \frac{Fn^4}{C_{FM0}} \qquad (8)$$

Fig. 6. C_{TM}/C_{FM0} vs Fn^4/C_{FM0} for KCS.

Fig. 8. Numerical $1 + k$ vs Fn for the KCS 1:79 and 1:75 of (Terziev et al., 2021).
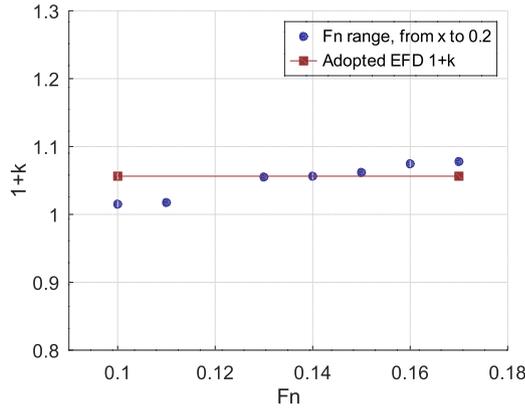

Fig. 7. Experimental form factor determination by using Prohaska's method, for different Froude number ranges considered (lower limit varied, upper limit fixed at $Fn = 0.2$), for the KCS model.

Table 4
Summary of CFD simulations for the KCS model at scale 1:79: froude and Reynolds numbers, estimated wall resolution (y^+), form factor $1 + k$, and grid convergence index (GCI). turbulence model: k-ω SST.

Fr	Re	y^+	$1 + k$	GCI [%]
0.020	3.19×10^5	0.32	1.015	0.12
0.040	6.37×10^5	0.91	1.022	0.06
0.060	9.56×10^5	1.70	1.039	0.04
0.080	1.28×10^6	2.64	1.101	0.01
0.100	1.59×10^6	3.71	1.141	0.09
0.120	1.91×10^6	4.90	1.218	0.07
0.140	2.23×10^6	6.21	1.308	0.00
0.160	2.55×10^6	7.61	1.314	0.01
0.180	2.87×10^6	9.12	1.289	0.01
0.200	3.19×10^6	10.71	1.254	0.04
0.220	3.51×10^6	12.39	1.214	0.08
0.240	3.82×10^6	14.16	1.182	0.11
0.260	4.14×10^6	16.00	1.154	0.13
0.280	4.46×10^6	17.92	1.131	0.20
0.300	4.78×10^6	19.92	1.118	0.09
0.320	5.10×10^6	21.98	1.118	0.43
0.340	5.42×10^6	24.12	1.117	0.35
0.360	5.74×10^6	26.32	1.114	1.06
0.380	6.06×10^6	28.59	1.118	1.86
0.400	6.37×10^6	30.93	1.117	1.09

where C_{FM0} is the ITTC-57 correlation line coefficient for the Rn of the model test and C_{TM} is the dimensionless total resistance of the model ship. From the experimental results we plot in Fig. 6 the left and right sides of Eq. (8) as data points (C_{TM}/C_{FM0}, Fn^4/C_{FM0}) for the KCS model. The dashed red vertical lines indicate the limits of the range $Fn = [0.1, 0.2]$, as recommended by the ITTC. The form factor can then be determined by linear regression. In this paper, the regression lines were obtained using the method explained by York (York et al., 2004).

Although the data points should align in a straight line for model speeds with $Fn < 0.2$, it is worth noting that at very low values of Fn, the measured points deviate from a straight line, making it necessary to select an appropriate data set to determine the form factor.

While Prohaska's method yields a unique value of $1 + k$ when applied over a fixed Fn range, in this study we applied the regression over different subsets of Froude numbers by varying the lower bound of the interval (while keeping $Fn = 0.2$ as the upper limit). This procedure allows us to illustrate the sensitivity of the estimated $1 + k$ to the chosen regression range and explains the multiple values presented in Figs. 7 and 12.

From Fig. 7 it could be observed that when the range of Fn is considered to be 0.1 to 0.2, the resulting value of $1 + k$ is found to be slightly lower than those obtained from a smaller range of Fn. This phenomenon can be attributed to the potential for laminarization of the flow at very low Rn. However, it could also be observed that the values found for $1 + k$ rapidly attain a stable value. As illustrated in Fig. 7, a horizontal line is drawn to indicate the $1 + k$ that is ultimately adopted as valid by the Prohaska method ($k_{ITTC} = 0.056$, for $Fn = [0.14, 0.20]$ and $Rn = [2.23e + 06, 3.18e + 06]$).
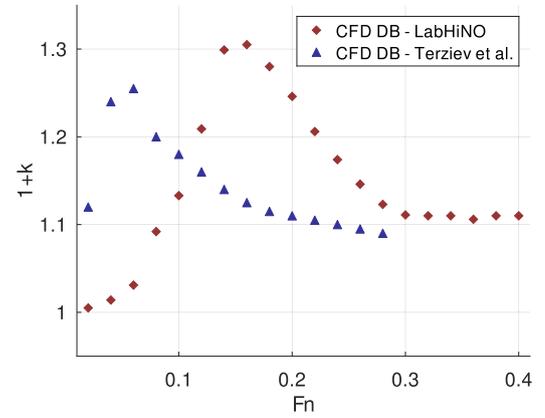
3.1.2. Numerical form factor determination

The CFD-based form factor method considered for this study follows assumptions (Hughes, 1954) and is derived using the relationship:

$$1 + k = \frac{C_F + C_{VP}}{C_{F0}} = \frac{C_V}{C_{F0}} \tag{9}$$

where the frictional drag coefficient (C_F) and the viscous pressure coefficient (C_{VP}) are obtained from the double-body CFD simulation. C_{F0} represents the equivalent flat plate resistance obtained from the same Rn as the calculations using the ITTC-57 correlation line.

To validate our numerical model, we compare our calculations with previous results presented by Terziev et al. (2021). Fig. 8 shows $1 + k$ vs Fn obtained by CFD DB for our numerical KCS model compared with Terziev et al. (2021) KCS numerical model, both using the same turbulence model. Table 4 presents a summary of CFD simulations for the KCS model at scale 1:79.

The mesh was designed so that the first off-wall cell partially resolved the near-wall region. As a consequence, the dimensionless wall distance spans approximately $0.3 \leq y^+ \leq 31$ over the tested Froude numbers. At low speeds, the first cell lies well inside the viscous sublayer or the lower part of the buffer region, while at the highest speeds it approaches the beginning of the logarithmic layer. This range is fully consistent with the kLowReWallFunction boundary condition used in OpenFOAM,
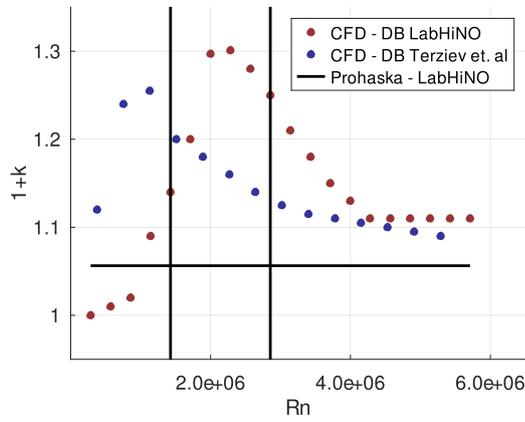
Fig. 9. Numerical $1 + k$ vs Rn for the KCS 1:79 and 1:75 of Terziev et al. (2021).

Fig. 10. $1 + k$ vs Rn for the KCS. numerical (CFD DB) and experimental results (EFD) from present work and from data set (Terziev et al., 2020).

Fig. 11. C_{TM}/C_{FM0} vs Fn^4/C_{FM0} for fishing vessel.

which provides a unified formulation for the turbulent kinetic energy k in both low- and high-Reynolds-number regimes by switching between viscous and logarithmic expressions depending on y^+ (OpenFOAM community, n.d.). In practical terms, the KCS simulations operate in a mixed near-wall-resolved regime for small y^+ and transition smoothly toward a classical wall-model behaviour as y^+ approaches $\mathcal{O}(30)$, a range widely recommended for log-law-based wall functions.

The behavior of $1 + k$ with Fn is analogous to that which has been previously documented. Moreover, it could be observed that an asymptotic value corresponding to that determined by Terziev et al. (2021) is attained for our model from $Fn \geq 0.30$.

Whilst there is a correspondence with asymptotic value it appears that our numerical model stabilizes at a higher Fn. However, if the same graph is shown as a function of Rn, it can be seen that both cases converge to a stable value of $1 + k$ around the same Rn (between $4e + 06$ and $5e + 06$). Fig. 9 shows $1 + k$ versus Rn obtained by CFD DB for the KCS on scale 1:79 and in scale 1:75 from Terziev et al. (2021).

Fig. 9 also shows the experimentally obtained value of $1 + k$. The vertical lines indicate for the 1:79 scale model the limiting values of $Fn = 0.1$ and $Fn = 0.2$.

It is evident that the EFD value of $1 + k$ differs significantly from the $1 + k$ values reported in the CFD DB model within the Fn range where the experimental value was obtained. However, the EFD value closely resembles the asymptotic value of the CFD DB, exhibiting a mere 5.1% discrepancy. Furthermore, it is noteworthy that the EFD value is not significantly different from the CFD DB value obtained for low Fn (for instance, it is merely 5.3% higher for $Fn = 0.02$).

3.1.3. EFD And CFD extended comparison of 1:79 KCS with the literature

We have previously compared our $1 + k$ results with Terziev et al. (2021) results since in that work they used the same turbulence model and a similar scale to ours. In this subsection, in order to reinforce the validity of our numerical model, we will compare our results with those of a large base compiled from existing literature (CFD and EFD). The dataset used for comparison was generated by Terziev et al. (2020) and includes a wide variety of turbulence models and scales.

Fig. 10 illustrates our $1 + k$ results (CFD and EFD) alongside those compiled by Terziev et al. (2020).

First of all, we can point out that the $1 + k$ EFD value obtained in our study aligns well with the corresponding values reported in the literature. In this way we have confidence in the use of our EFD value as a reference to validate our numerical model.

On the other hand, with respect to our CFD DB model, it is interesting to note that the values found for $1 + k$ for the lowest Rn and for the highest Rn correspond well with the $1 + k$ CFD values found in the literature.

It is worth mentioning, in turn, that the observed peak in the values of $1 + k$ also appears in the results of Terziev et al. (2020) for a
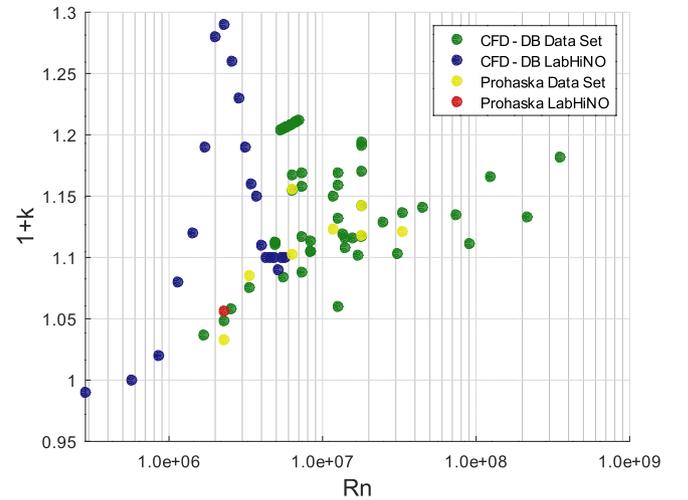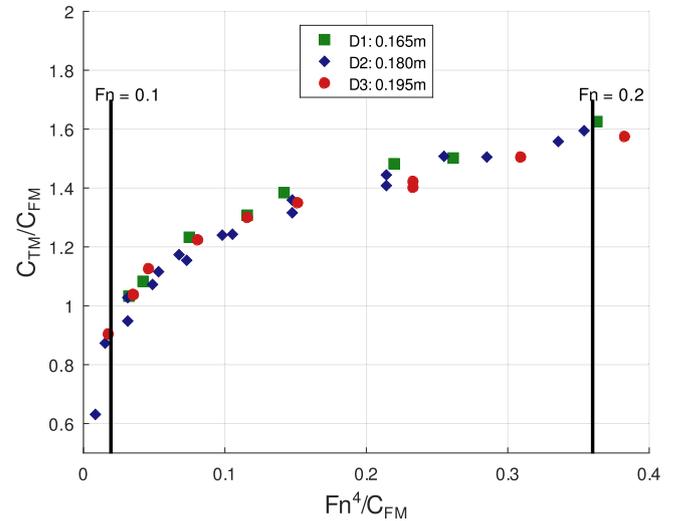
variety of turbulence models and scales, and is directly associated with the turbulence transition modeling. Despite the fact that the turbulence model in CFD simulations can significantly influence the prediction of the form factor, particularly at low Rn where laminar-to-turbulent transition occurs, Fig. 10 shows that our model could adequately reproduces the behavior of $1 + k$ with Rn.

So, given the previous results, we are confident that we can obtain valid results for the form factor by means of EFD (applying the Prohaska method) and by means of CFD using the double-body method and considering the lowest and highest values of the model's Rn range.

3.2. Fishing vessel form factor

3.2.1. Experimental form factor determination

Having validated our CFD DB numerical model and having confidence in the accuracy of our experimental measurements, the following subsection analyses the results for the form factor of the fishing vessel under study, using EFD and CFD.

Fig. 11 shows the $(C_{TM}/C_{FM0}, Fn^4/C_{FM0})$ points at three different draughts for the fishing vessel.

As mentioned in previous sections, in the previous study Oyuela et al. (2024) three distinct draughts were analyzed; however, in the present work we will concentrate on the results of $1 + k$ for the largest draughts
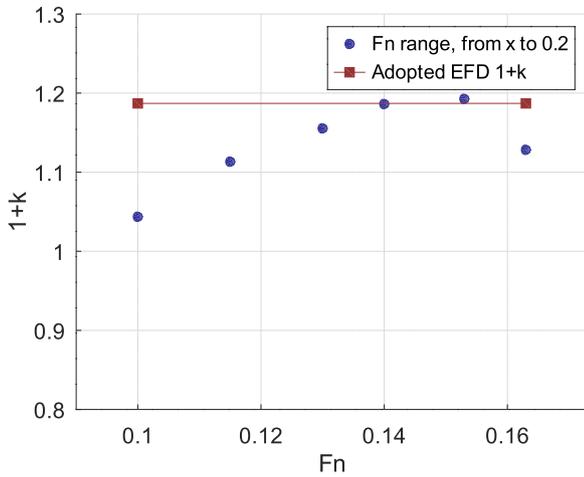
Fig. 12. Experimental form factor determination by using Prohaska's method, for different Froude number ranges considered (lower limit varied, upper limit fixed at $Fn = 0.2$), for the fishing vessel at D = 0.195 m.
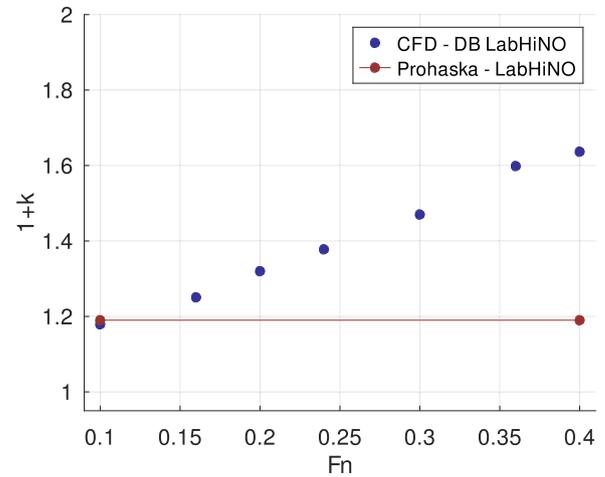

Fig. 13. Numerical and experimental $1 + k$ vs Fn for the fishing vessel.

previously examined (draught 0.195 m). It should be noted that this draught was selected solely for the purpose of streamlining the presentation of results, and the observations made for this specific draught are applicable to the other two draughts.

As was done for the KCS, Fig. 12 shows the values of $1 + k$ obtained for different data sets for the fishing vessel. The abscissa axis indicates the initial value of Fn that was taken into consideration for each data set. In all cases, the final value of Fn that was considered was $Fn = 0.2$. The value of $1 + k$ is more dependent on the range of Fn considered than the presented for the KCS. This phenomenon could be ascribed to the fact that Rn of the model is reduced for the fishing vessel, thereby increasing the probability of flow separation and impeding the transition of the boundary layer to turbulence. However, this phenomenon may also be related to the hull shapes, which are significantly different from each other.

Fig. 12 also shows a horizontal line indicating the $1 + k$ that is ultimately adopted as valid by the Prohaska method for the fishing vessel ($k_{ITTC} = 0.187$, for $Fn = [0.15, 0.20]$ and $Rn = [9.61e + 05, 1.28e + 06]$).

As expected, the value of the form factor for this type of vessel is much higher than that of the KCS.

3.2.2. Numerical form factor determination

Fig. 13 shows $1 + k$ vs Fn obtained by CFD DB for the model scale fishing vessel and also includes the EFD $1 + k$ value obtained by Prohaska method. Table 5 shows a summary of CFD simulations for all geometric scales.

As four geometric scales were simulated using dynamically similar meshes, this naturally leads to very small wall-unit values at the smallest model scale and progressively larger values as the Reynolds number increases. The resulting mean wall distances range from $y^+ \approx 0$ at the lowest speeds up to $y^+ > 300$ in the largest/full-scale cases. This behaviour is expected: at model scale, the boundary layer is mostly resolved (low-y^+ regime), whereas at full scale the first off-wall cells lie predominantly within the logarithmic layer, which is the intended operating range of standard wall-function approaches (typically $30 \lesssim y^+ \lesssim 300$). Although the full-scale simulations reach mean y^+ values exceeding 300, these cases do not alter the qualitative behaviour of the form-factor curve. The largest-y^+ conditions do not introduce any change of slope or anomalies in the $1 + k$–Re relation, and the overall conclusions regarding scale effects remain robust.

Contrary to what was observed for the KCS, an asymptotic value of $1 + k$ is not reached for the fishing vessel case. Furthermore, as Fn increased, the value of $1 + k$ CFD DB became increasingly distant from the experimental value obtained.

Table 5
Summary of CFD simulations for all geometric scales: Reynolds number, near-wall resolution (y^+), form factor $1 + k$, and grid convergence index (GCI) for each froude number. turbulence model: k-ω SST.

Fr	1:20	1:10	1:5	1:1
Reynolds number				
0.100	6.40×10^5	1.81×10^6	5.12×10^6	5.73×10^7
0.160	1.02×10^6	2.90×10^6	8.20×10^6	9.17×10^7
0.200	1.28×10^6	3.62×10^6	1.02×10^7	1.15×10^8
0.240	1.54×10^6	4.35×10^6	1.23×10^7	1.37×10^8
0.300	1.92×10^6	5.43×10^6	1.54×10^7	1.72×10^8
0.360	2.31×10^6	6.52×10^6	1.84×10^7	2.06×10^8
0.400	2.56×10^6	7.25×10^6	2.05×10^7	2.29×10^8
Near-wall resolution (y^+)				
0.100	0.40	1.30	12.0	108
0.160	0.70	9.00	17.0	168
0.200	1.03	11.0	22.0	207
0.240	1.40	11.4	26.0	245
0.300	2.23	12.6	32.0	302
0.360	2.70	14.6	38.0	353
0.400	3.00	15.9	41.0	389
Form factor ($1 + k$)				
0.100	1.179	1.399	1.489	1.654
0.160	1.251	1.622	1.484	1.690
0.200	1.320	1.570	1.501	1.713
0.240	1.378	1.513	1.522	1.714
0.300	1.470	1.465	1.528	1.727
0.360	1.598	1.465	1.548	1.731
0.400	1.637	1.473	1.554	1.745
Grid Convergence Index (GCI) [%]				
0.100	0.028	0.773	1.748	0.002
0.160	0.112	1.032	0.005	0.849
0.200	0.009	3.722	0.859	3.730
0.240	0.003	2.193	0.723	3.985
0.300	0.002	0.001	3.544	1.681
0.360	1.382	0.003	0.311	2.053
0.400	13.433	0.011	0.090	4.421

The present study reinforces the earlier finding at Oyuela et al. Oyuela et al. (2024) of the dependence of $1 + k$ on Fn, as observed for Fn values of 0.1 and 0.2. This verification is conducted over the entire range of Fn values encompassed by the model.
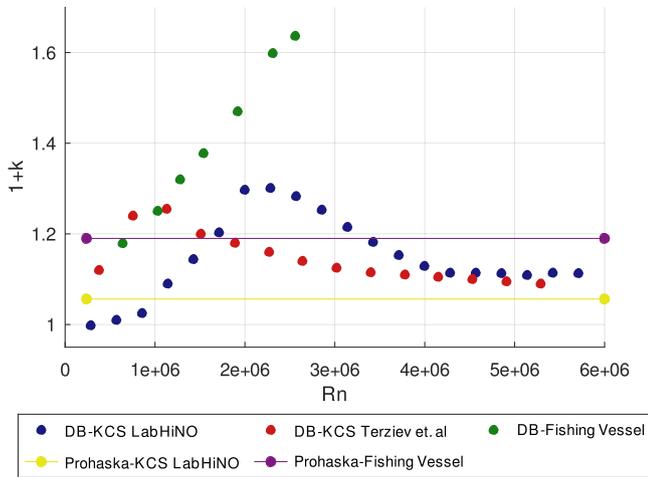
Fig. 14. Numerical and experimental $1 + k$ vs Rn for the KCS and the fishing vessel.

Fig. 15. $1 + k$ vs Rn for the KCS and the fishing vessel (FV). KCS numerical (CFD DB) and experimental results (EFD) from present work and from Data set (Terziev et al., 2020). Fishing vessel numerical (CFD DB, considering different scales) and experimental results (EFD) from present work. Logarithmic scale.

3.3. Comparison of $1 + k$ for the fishing vessel and KCS model

To highlight the distinctive behavior of $1 + k$ vs Rn that we have found for the fishing vessel, in this subsection we compare this behavior with that for the KCS. Firstly, for the purposes of enhanced analytical clarity, the results of Figs. 9 and 13 are herein presented in Fig. 14.

Fig. 14 shows $1 + k$ vs Rn obtained by CFD DB for the KCS in scale 1:79, the KCS in scale 1:75 from Terziev et al. (2021) and the fishing vessel in model scale (1:20). The graph also shows the EFD values of $1 + k$ obtained by Prohaska's method in the present work (for the KCS in scale 1:79 and the fishing vessel).

It is evident that within the specified model speed range, the fishing vessel does not attain an asymptotic value of $1 + k$, as observed in the KCS. Therefore, and in contrast to the behavior exhibited by the KCS, the EFD value of $1 + k$ for the fishing vessel diverges increasingly from the value calculated through utilization of the CFD DB model, as the model speed increases.

It is remarkable that even considering the highest model speed, the fishing vessel does not reach Rn values similar to those that produced the stabilization of the $1 + k$ value in the case of the KCS (Rn between $4e + 06$ and $5e + 06$).

So, to better understand the behavior of $1 + k$ with Rn in the case of the fishing vessel, CFD DB calculations of $1 + k$ have been performed for different model scales in order to consider a higher Rn range. We have evaluated the 1:20 scale and three different scales, 1:10, 1:5 and 1:1, that will plot the scale's influence on this research.

Fig. 15 illustrates our $1 + k$ results (CFD DB and EFD) in conjunction with the results collated in the existing literature for the KCS and our $1 + k$ results (CFD, considering different scales, and EFD) for the fishing vessel.

In Fig. 15 it can be observed that our CFD DB model presents, for both studied vessels, a peak approximately for the same Rn range. This peak could be directly associated with the modeling of the transition.

On the other hand, it could be observed that while the variation of $1 + k$ with Rn diminishes for higher values of Rn for both vessels, the fishing vessel does not attain an asymptotic value as distinctly as the KCS.

The impact of Rn on the value of $1 + k$ is considerably more substantial for the fishing vessel than for the KCS. To illustrate this, the disparity between the $1 + k$ value at low Rn and high Rn is approximately 40% for the fishing vessel, whereas for the KCS it is approximately 8%. Furthermore, the fishing vessel possesses a terminal value of $1 + k$ that is almost 50% higher than that of the KCS.
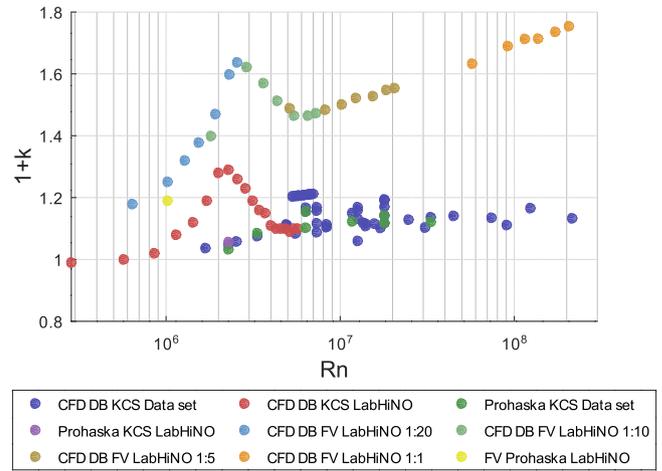
4. Analysis

In this section, the behavior of the form factor of the fishing vessel with respect to Rn is analyzed. The analysis begins with a clarification of Rn vs Fn effects, then it considers the effect of the frictional line, followed by the force decomposition, the pressure distribution on the hull, and the influence of the L/B ratio. We conclude the section by analyzing the effect of the large variation of $1 + k$ with Rn on the fishing vessel's total resistance and effective power prediction.

4.1. Clarification of reynolds-number vs. froude-number effects

To disentangle the influence of Reynolds and Froude numbers on the form factor, it is important to distinguish between linear scaling and viscous scaling, following the terminology of Terziev et al. (2021). In viscous scaling, Rn is held constant while Fn is varied, allowing a direct assessment of Fn on $1 + k$. In contrast, our simulations were performed under linear scaling, so changes in speed necessarily translate into simultaneous changes in both Rn and Fn, which precludes a clean separation of their individual contributions.

Nevertheless, our results provide strong evidence that the dependence of $1 + k$ is governed by Reynolds number. This conclusion is supported by the agreement between our CFD-DB predictions for the KCS and those reported by Terziev et al. (2021), who demonstrated that the strong variation of $1 + k$ at low speeds is mainly related to transition-modelling effects at low Rn. Consistent behaviour has also been reported in a wide range of studies employing different turbulence models and geometric scales Terziev et al. (2020), reinforcing the generality of this trend.

Furthermore, all CFD-DB simulations in this study were performed with fixed trim and sinkage. Since gravitational effects associated with Fn are suppressed under these constraints, the observed variations of $1 + k$ with speed can only arise from viscous processes, i.e. from changes in Reynolds number. This provides additional confirmation that Rn, rather than Fn, is the parameter controlling the behaviour of the form factor in the present investigation.

4.2. Selection of the frictional line

Numerical friction lines derived from CFD simulations of flat plates offer an alternative to the ITTC-57 correlation line. Using numerical friction lines reduces the speed dependency of the form factor, specially at low Rn Korkmaz et al. (2021).
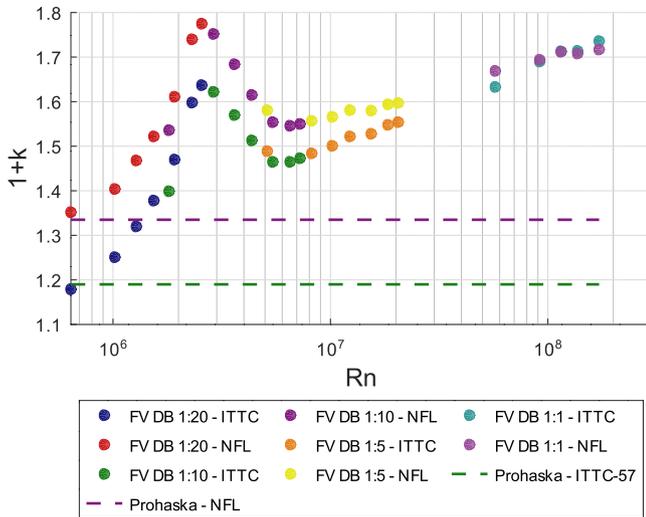
Fig. 16. $1 + k$ vs Rn for the fishing vessel (FV) with two different friction lines.

Fig. 17. Force coefficients C_T, C_{VP} and C_F obtained from numerical CFD DB and the ITTC-57 correlation line represented by C_{F0} vs Rn for the fishing vessel.

Fig. 16 shows $1 + k$ vs Rn for the fishing vessel for two different friction lines. We compare $1 + k$ values obtained with the ITTC-57 model-ship correlation line Committee (2011), with those obtained using a numerical friction line (NFL) proposed by Korkmaz et al. (2019).

Considering the numerical frictional line produces higher values of $1 + k$ for the lower Rn, the prediction based on the CFD approach clearly gives smaller variation of form factor, which should better represent the realistic Rn dependence of form factor. However, the difference is still significantly larger than that found for the KCS. In fact, the disparity between the $1 + k$ value at low Rn and high Rn is still approximately 25% for the fishing vessel considering the NFL.

It is remarkable that the value of $1 + k$ for higher Rn (i.e scale 1:1) is practically equivalent, irrespective of the frictional line under consideration. This is to be expected, since the differences between frictional lines occur primarily at low Rn.

To summarize, the strong dependence of $1 + k$ on Rn and the high terminal value of $1 + k$ observed for the fishing vessel cannot be attributed to the frictional line selection.

4.3. Force decomposition

Fig. 17 shows the total resistance coefficient (C_T), the frictional drag coefficient (C_F) and the viscous pressure coefficient (C_{VP}) obtained from the double-body CFD simulation for the fishing vessel, as a function of Rn. It also shows the ITTC-57 correlation line (C_{F0}).

It is evident that the frictional drag coefficient (C_F) of the CFD DB model exhibits a high degree of similarity with the ITTC-57 correlation line (C_{F0}) for Rn values greater than $5e + 06$, (i.e. beyond the transition region). Regarding C_{VP}, its value decreases very slowly with Rn, resulting in a consistent augmentation of $1 + k$ with Rn, as illustrated in Fig. 16. Moreover, the rate at which $1 + k$ increases with Rn diminishes as Rn increases, primarily due to the plateaus observed in C_F.

To illustrate the characteristic behavior of the C_{VP} on the fishing vessel, Fig. 18 shows the frictional drag coefficient (C_F) and the viscous pressure coefficient (C_{VP}) obtained from the double-body CFD simulation for the fishing vessel and the KCS.

We can appreciate in Fig. 18 that the C_{VP} value for the fishing vessel is more than three times the C_{VP} value for the KCS over the entire Rn range considered. Moreover, the value of C_{VP} seems to be decreasing much more slowly, with Rn, for the fishing vessel than for the KCS.

In contrast to the friction resistance coefficient, C_{VP} appears to be less sensitive to variations in Rn number; however, it is significantly influenced by the hull form.
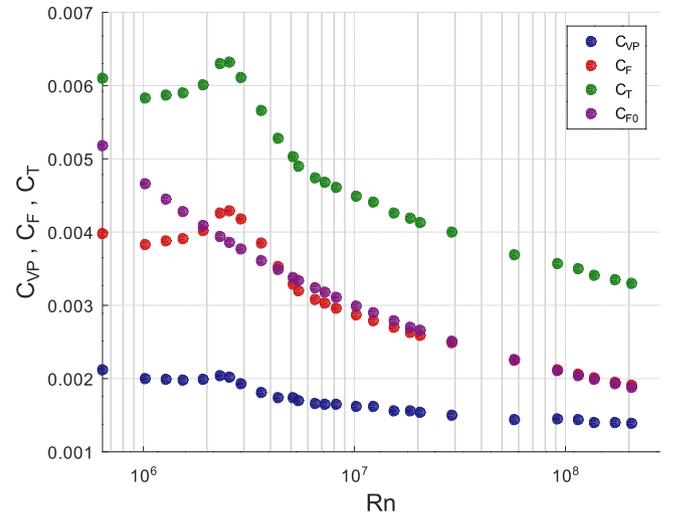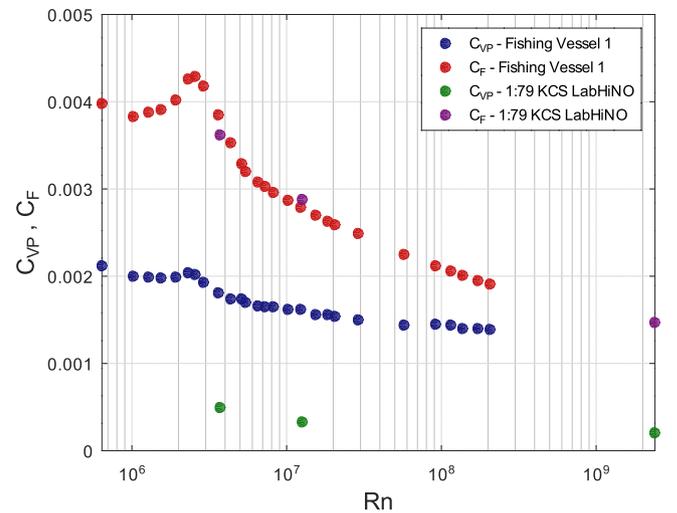

Fig. 18. C_{VP} and C_F, obtained from numerical CFD DB, vs Rn for the fishing vessel and the 1:79 KCS LabHiNO.

To better understand the strong influence of hull form on the behavior of $1 + k$ with Rn, it is necessary to consider the two competing mechanisms that contribute to the viscous pressure resistance (and hence to the form factor). First, the three-dimensional boundary layer (BL) contribution, second, the contribution from vortical structures generated by a blunt/transom stern. The BL contribution decreases with increasing Rn because the BL thins and viscous kinetic-energy dissipation along the hull path is reduced. The contribution of the vortex structures could increase or remain more or less stable as Rn increases. The net C_{VP} (Rn) curve results from the superposition of these opposite trends (BL vs vortex). Similar dual-mechanism interpretations are reported in Zeng et al. (2019) and Raven (2016) and are consistent with wetted-transom scaling studies Korkmaz et al. (2022).

Specifically for the ship considered in the present work Fig. 19 shows contours of longitudinal velocity profiles U_X/U_0 in a plane located at $x/L = 0.05$, abaft the stern section at model and full scale Rn $log(Rn) = 06$, 08 respectively) and $Fn = 0.2$. As expected the BL thins with Rn reducing viscous dissipation as Rn increases. On the other hand, Fig. 20 shows Q-criterion isosurfaces (Q = const) showing the vortex system shed from the transom at model and full scale Rn ($log(Rn) = 06$, 08) and $Fn = 0.2$. Fig. 20 also shows some streamlines in order to highlight flow recirculation zones. It seems that the contribution of the
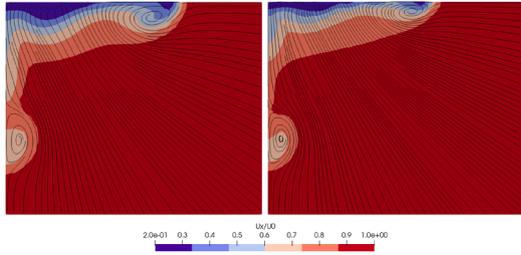
Fig. 19. Contours of longitudinal velocity profiles U_X/U_0 in a plane located at $x/L = 0.05$, abaft the stern section at model (left) and full (right) scale Rn ($log(Rn) = 6, 8$ respectively) and $Fn = 0.2$.
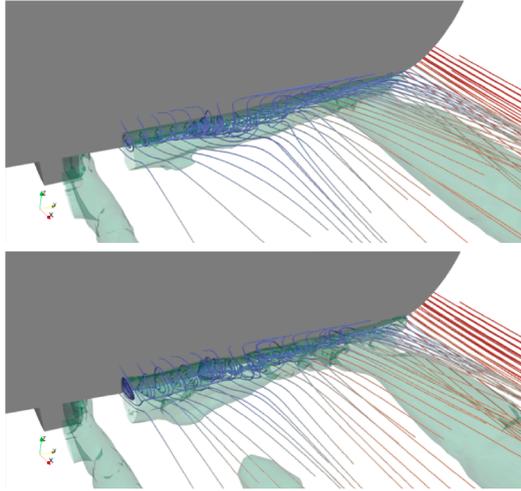

Fig. 20. Q-criterion isosurfaces (Q = 10), showing the vortex system shed from the transom at model (upper) and full scale (lower) Rn ($log(Rn) = 6, 8$ respectively) and $Fn = 0.2$.

vortex structures remain more or less stable with Rn for the fishing vessel. We can conclude that the large vortex structures observed for the fishing vessel are responsible for its high C_{VP} value. In turn, the fact that these structures remain stable with Rn explains the slight dependence of C_{VP} on Rn. The small decrease in C_{VP} with Rn observed can be attributed to the superimposed effect of the reduction in BL.

4.4. Pressure distribution on the hull

In this section we discuss the results from the pressure distribution (C_P) on the hull for the fishing vessel and considering different scales. This dimensionless parameter is defined as:

$$C_P = \frac{p - p_\infty}{\frac{1}{2}\rho V^2} \tag{10}$$

where p is the pressure in the hull, p_∞ is the pressure in the undisturbed incident flow, V is the vessel velocity, ρ is the water density. It is important to note that the C_{VP} value is obtained from the integration and the projection in the forward direction of the model of the C_P value. Therefore, an analysis of the pressure distribution at different scales will allow us to better understand the behavior of C_{VP} with Rn.

Figs. 21–24 show the dimensionless pressure distribution (C_P) on the hull of the fishing vessel for both the experimental model scale (1:20) and the full-scale (1:1) case, at a Fn of 0.2, from different viewing angles.

It is appreciated that the pressure recovery in the stern area of the vessel is considerably lower than that observed for more hydrodynamic vessels (such as the KCS Song et al., 2019), which accounts for the high value of $1 + k$ for this type of vessel. On the other hand, considering the Rn effect on C_P, it has been observed that there is a very slight difference in pressure distribution in the stern area for the different scales. In fact,
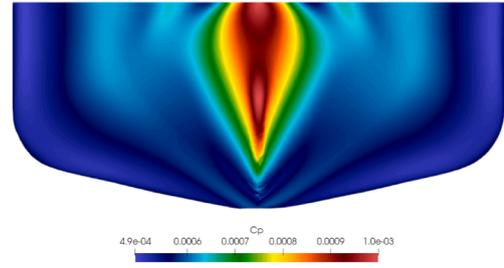

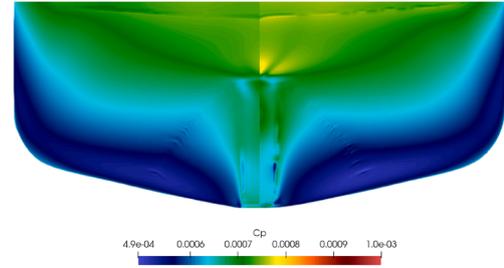**Fig. 21.** Cp for $Fn = 0.2$ - View from the bow - Left: scale 1:20. Right: scale 1:1. fishing vessel.

Fig. 22. Cp for $Fn = 0.2$ - View from the stern - Left: scale 1:20. Right: scale 1:1. fishing vessel.
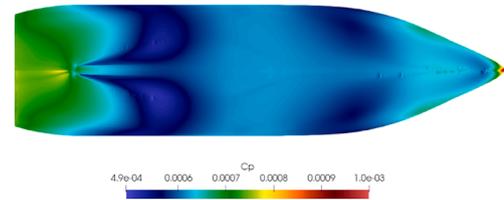

Fig. 23. Cp for $Fn = 0.2$ - View from the bottom - Top: scale 1:20. bottom: scale 1:1. fishing vessel.
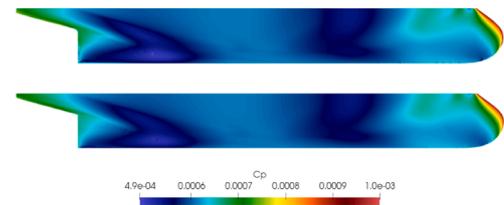

Fig. 24. Cp for $Fn = 0.2$ - View from the side -Up : scale 1:20. Down: scale 1:1. fishing vessel.

the pressure for the 1:1 scale recovers slightly more than that for the 1:20 scale, which is consistent with the observed very slight decrease of C_{VP} with Rn for the studied vessel.

Fig. 25 presents the longitudinal distribution of the pressure coefficient ($C_P(x/L)$) at various Reynolds numbers and for multiple waterplanes (i.e., horizontal slices at constant z/T). The longitudinal coordinate is expressed as x/L, where $x/L = 0$ corresponds to the forward perpendicular. The results show that the fishing vessel exhibits a persistent pressure deficit in the stern region across all Reynolds numbers, with only negligible variations between scales. The difference in stern pressure between the model scale ($Rn = 1.3e + 6$) and full scale ($Rn = 1.1e + 8$) is approximately ($\Delta C_P = .01$-0.02), indicating that aftbody pressure recovery is weak and largely insensitive to flow inertia. These quantitative findings are fully consistent with the observed slow decay of C_{VP} with Reynolds number, supporting the conclusion that viscous pressure losses in the stern region dominate the behavior of the form factor $1 + k$ for this hull form.
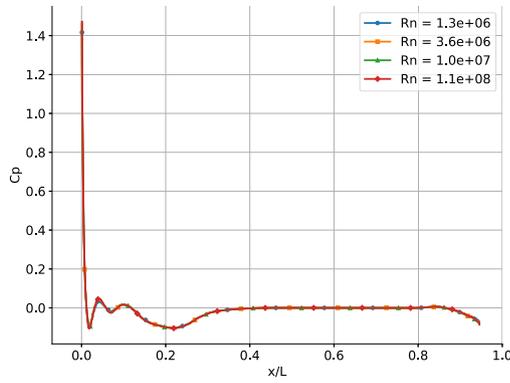
(a) Pressure coefficient distribution $C_p(x/L)$ along the z/T = 0 waterline.
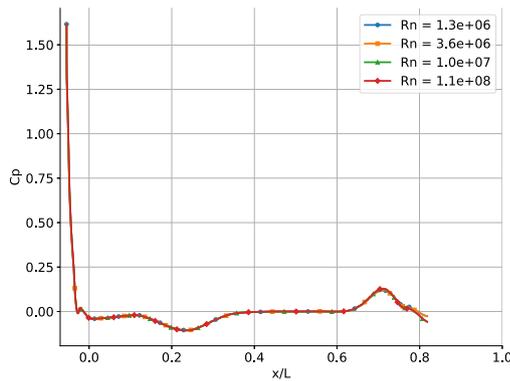
(b) Pressure coefficient distribution $C_p(x/L)$ along the z/T = 0.5 waterline.
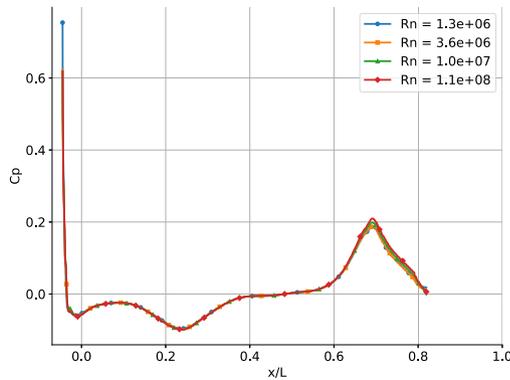
(c) Pressure coefficient distribution $C_p(x/L)$ along the z/T = 0.75 waterline.

Fig. 25. Distribution of $C_p(x/L)$ along multiple waterlines for different Reynolds numbers, showing a consistent stern pressure deficit and only minor scale-induced variations.

4.5. Effect of the L/B ratio

The vessel under study exhibits a high C_{VP} values, which is associated with the difficulty of the flow in recovering the pressure value in the stern area. Furthermore, the C_{VP} values exhibit a very weak dependence on Rn. These characteristics are closely linked, since the energy loss of flow due to viscosity, in this particular type of vessel, is so large that despite the increase in inertia of the flow with increasing Rn, no
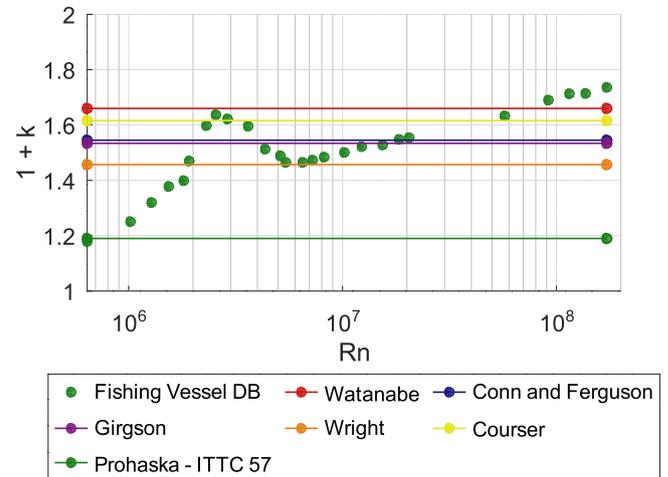

Fig. 26. $1 + k$ vs Rn for the fishing vessel. CFD DB, EFD from present work, and $1 + k$ from different empirical formulae Molland et al. (2017), Conn and Ferguson (1968), Grigson (2000), Wright (1984), Couser et al. (1997).

significant pressure recovery (and hence no significant C_{VP} drop) with Rn is observed.

The behavior of C_{VP} with Rn is pivotal in comprehending the behavior of $1 + k$ with Rn on a specific ship type, as the behavior of C_F with Rn is less dependent on the hull type under consideration. Thus, the arguments presented so far provide a solid basis for justifying the significant influence of the Rn on the value of $1 + k$ for the fishing vessel under investigation.

However, to the best of our knowledge, we have not identified in the extant literature such a high value of $1 + k$ as the one observed for the fishing vessel in the 1:1 scale (i.e. $1 + k = 1.73$ for $Rn = 1.72e + 08$). For instance, we have considered several empirical formulae for $1 + k$ based on model tests. Fig. 26 shows the $1 + k$ values obtained with CFD DB for the fishing vessel vs Rn, horizontal lines with the $1 + k$ values calculated by using different empirical formulae Molland et al. (2017), Conn and Ferguson (1968), Grigson (2000), Wright (1984), Couser et al. (1997) and the EFD $1 + k$ value obtained using Prohaska's method.

From Fig. 26 it's clear that the values of $1 + k$ obtained by empirical formulae are widely dispersed and that it is impossible to clearly determine which of them should be selected in order to perform an extrapolation process. It should be noted that the empirical formulae used have, as input, different main dimensions of the vessel ($C_B, L/B, B/T, S/L^2, L/\nabla^{1/3}$) and a range of validity. In all cases our fishing vessel has a L/B value that deviates from the empirical formulae limits of applicability.

Consequently, these two facts (not finding a value of $1 + k$ close to that found for CFD DB at 1:1 scale, and not being within the validation range of application of the formulas) guided the decision to explore results in the literature related to flow around completely submerged bodies (since it is a case analogous to DB, without free surface effect).

A classic empirical drag estimation method in aircraft aerodynamics, to approximate aircraft fuselage drag, consists in multiplying a flat-plate fully turbulent skin friction coefficient with a form factor (FF) and considering the fuselage's wetted area. The fully turbulent skin friction coefficient only depends on the Rn and the form factor is an empirical equation based on a certain geometrical characteristic that should account for the fuselage's pressure drag. The aircraft's fuselage is approximated by a streamlined body of revolution. Hoerner Hoerner (1965) was the first to derive a purely empirical form factor for bodies of revolution based on correlations with a limited amount of wind tunnel experiments. The fuselage body's fineness ratio (l/d) is the primary variable in the form factor equation. Hoerner's available experimental data allowed the derivation of a form factor valid only for $\frac{l}{d} > 4.5$, which
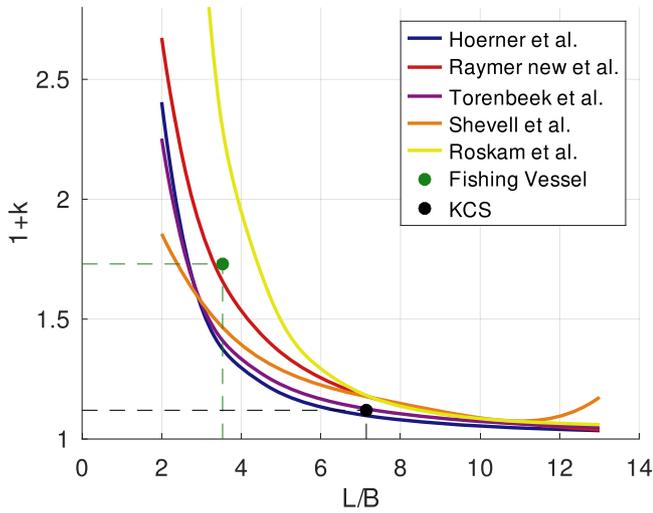
Fig. 27. Form factors for streamlined bodies vs fineness ratio (l/d) (data from Refs. Hoerner (1965), Raymer (2019), Torenbeek (2010), Roskam (1987), Shevell (1989) and CFD DB $1 + k$ obtained in the present work for the fishing vessel in scale 1:1 and for the KCS from Terziev et al. (2020).

was then extrapolated to smaller $\frac{l}{d}$ without experimental proof of the form factor's validity. Since the initial derivation by Hoerner, several researchers (e.g., Raymer, 2019; Torenbeek, 2010; Roskam, 1987; Shevell, 1989) continued adjusting form factors for bodies of revolution to approximate aircraft fuselage drag and extending the range of validity to smaller values of l/d.

Fig. 27 shows different curves of form factors vs fineness ratio (l/b) obtained from Hoerner (1965), Raymer (2019), Torenbeek (2010), Roskam (1987), Shevell (1989) for streamlined bodies. Fig. 27 also shows the CFD DB $1 + k$ obtained in the present work for the fishing vessel in scale 1:1 and from collected CFD DB values for the KCS Terziev et al. (2020).

These last two values were plotted for l/d = 3.50 and l/d = 7.14 corresponding to the L/B values for the fishing vessel and the KCS respectively.

Based on the previous results, the value of $1 + k$ for the KCS is in close alignment with Hoerner's curve, which was determined for large l/d values. In contrast, the value of $1 + k$ for the fishing vessel exhibits a stronger correlation with the "Raymer New" curve which was adjusted to better match the form factors for lower l/d ratios Raymer (2019).

It is interesting to note the correct fit of our $1 + k$ CFD DB values with data that, although originated from another field of study, included values of l/d (L/B for the vessel) low enough to include the L/B of our vessel under study.

4.6. Effect of the value of $1 + k$ on total resistance and effective power prediction

We conclude the section by analyzing the effect of the large variation of $1 + k$ with Rn on the fishing vessel's total resistance and effective power prediction.

The results of the towing tank tests could be extrapolated to estimate the total resistance and effective power of the full-scale ship by using the ITTC performance prediction method (Committee, 2017). The total ship resistance coefficient can be calculated as:

$$C_{TS} = (1 + k_S)C_{FS0} + C_W + \Delta C_F + C_A \tag{11}$$

where C_{TS} and C_{FS0} are the total resistance and the frictional resistance coefficients force ship respectively. The subscript S refers to the ship (scale 1:1) in contrast to the subscript M which refers to the model (physical model used in the towing tank).

C_{FS0} is calculated by using the ITTC 1957 correlation line and considering the ship Rn number. k_S is the ship form factor and C_W is the wave resistance coefficient.

A roughness allowance (ΔC_F) is applied to account for the relative increase in frictional resistance from model-scale to full-scale vessels, and a correlation allowance (C_A) is applied to account for remaining differences between model-scale and full-scale vessels. Both, (ΔC_F) and C_A, were calculated according to [Committee (2017)]. The (ΔC_F) allowance depends on the full scale equivalent sand roughness (we adopted the standard value of 150 μm), waterline length (L_{WL}) and Rn. The C_A allowance depends only on the full-scale Rn. This method assumes that the wave resistance coefficient (C_W) is the same for the ship and the model and can be calculated as:

$$C_W = C_{TM} - (1 + k_M)C_{FM0} \tag{12}$$

where C_{TM} is the total resistance coefficient for the model (obtained by towing tank experiments) and C_{FM0} is the frictional coefficient for the model calculated by using the ITTC 1957 correlation line with the model Rn number. This method also assumes that the ratio of the viscous pressure resistance coefficient to the frictional resistance coefficient is constant, so that the form factor is constant (i.e. $k_M = k_S$).

The actual, total resistance of the ship without a propulsor (the bare hull) in calm water is obtained by multiplying the total resistance coefficient C_{TS} with dynamic pressure and wetted surface (S_S).

$$R_{TS} = \frac{1}{2}\rho V_S^2 S_S C_{TS} \tag{13}$$

The effective power needed to tow the vessel is defined by the work done per unit time which is equivalent to force times ship velocity.

$$P_{ES} = R_{TS} V_S \tag{14}$$

To show the effect of the selected value of k on the total ship resistance and the effective power, it is shown in Table 6 the estimated C_{TS}, R_{TS} and P_{ES} considering three different approaches or methods, to determine the value of k_M and k_S.

The first approach (method 1) is the classical ITTC approach, which considers $k_M = k_S$ and the form factor is obtained with Prohaska EFD method. The second approach (method 2) is the combined CFD-EFD method, which considers different values of k_M and k_S, calculated with the CFD DB model as proposed by Korkmaz et al. (2022). And finally we have also considered a third approach (method 3) in which $k_M = k_S = 0$. In Table 6 C_{TS}, R_{TS} and P_{ES} were calculated for two typical operational fishing vessel velocities. The table also shows the percentage differences in estimated effective power when methods 2 and 3 are compared with the ITTC method (method 1).

The third approach is typically employed when the form factor cannot be accurately determined using the experimental method, which leads to an overestimation of the effective power-about 5% in our case. In contrast, when the two-velocity CFD double-body (DB) form factor approach (method 2) is used, the estimated effective power is approximately 15% higher than that obtained using the traditional ITTC method.

Results indicate that the percentage differences in power estimation between the ITTC method and the proposed 2-k numerical method are sufficiently significant to warrant validation through sea trials in future work.

It is worth mentioning that the empirical formulas introduced from the aerospace field, as discussed in Section 4.4, could potentially be employed as a preliminary estimation tool for the k_s value, thereby circumventing the need for full-scale CFD calculations. It would be particularly valuable to establish a curve similar to those shown in Fig. 27, depicting $1 + k$ versus length-to-beam ratio (L/B) for fishing vessels, especially in the low L/B range. Such a curve would enable the implementation of a dual-k extrapolation method, where k_m is obtained from DB CFD at model scale, and k_s is derived from the referenced correlation. The values obtained using this method will be similar to those shown for Method 2 in Table 6.

Table 6

C_{TS}, R_{TS} and P_{ES} estimated considering three different approaches to determine the value of k_M and k_S.

Fn	v_S [m/s]	v_S [kn]	Method 1 (EFD)			Method 2 (EFD-CFD)			Method 3 ($k = 0$)			2 vs 1	3 vs 1
			C_{TS}	R_{TS} [kN]	P_{ES} [kW]	C_{TS}	R_{TS} [kN]	P_{ES} [kW]	C_{TS}	R_{TS} [kN]	P_{ES} [kW]	ΔP_{ES} %	ΔP_{ES} %
0.26	4.71	9.16	6.28	32.16	151.51	7.33	37.53	176.79	6.70	34.27	161.46	16.7	6.6
0.30	5.34	10.38	7.68	50.46	269.34	8.71	57.22	305.45	8.08	53.08	283.34	13.4	5.2

5. Conclusions

The dependence of the form factor k on the Reynolds number for the fishing vessel has been found to differ significantly from that observed for the KCS benchmark hull. Notably, the scale effect on the value of $1 + k$ is considerably more pronounced for the fishing vessel. Specifically, the discrepancy between $1 + k$ at model scale and full scale is approximately 40% for the fishing vessel, compared to only 8% for the KCS.

Moreover, although the rate of change of $1 + k$ with Rn decreases at higher Reynolds numbers for both vessels, the fishing vessel does not exhibit a clear asymptotic behavior as observed in the KCS. Additionally, the terminal value of $1 + k$ for the fishing vessel is nearly 50% greater than that of the KCS.

This distinct behavior of k with respect to Rn in the fishing vessel is primarily governed by the variation of the viscous pressure coefficient C_{VP}, rather than the frictional drag coefficient C_F, which remains nearly identical for both hull types across the range of Rn examined. Unlike C_F, which is relatively insensitive to hull geometry, C_{VP} appears to be strongly influenced by the form of the hull. Across the entire range of Rn, the values of C_{VP} for the fishing vessel are consistently higher than those observed for the KCS. This behavior is attributed mainly to reduced pressure recovery in the stern region of the fishing vessel, where the geometry induces significant viscous energy losses in the flow.

Furthermore, the decrease of C_{VP} with increasing Rn occurs much more gradually in the fishing vessel than in the KCS. This suggests that the viscous losses at the stern are sufficiently dominant in the fishing vessel that increased flow inertia at higher Rn does not yield substantial pressure recovery. The combination of a higher absolute value of C_{VP} and a weaker dependence on Rn explains the pronounced divergence in the behavior of $1 + k$ with Rn between the fishing vessel and the KCS.

Given that scale effects on the form factor are predominantly dictated by hull geometry, a comparative analysis was conducted between the $1 + k$ values obtained from our computational fluid dynamics (CFD) database for the fishing vessel at full scale and those derived from a series of empirical formulations. These formulations are based on various expressions of the three-dimensional characteristics of hull geometry. However, the values of $1 + k$ obtained using empirical methods derived from model tests exhibit wide variability, complicating the selection of a reliable expression for estimating $1 + k$ for the fishing vessel under investigation.

Among the geometric parameters defining hull form -such as C_B, L/B, B/T, S/L^2 and $L/\nabla^{1/3}$- the length-to-beam ratio L/B deviates most significantly from the values typically found in conventional ships. Consequently, a classical empirical drag estimation method from the field of aircraft aerodynamics was employed. In this method, the fineness ratio of the fuselage body l/d is the principal variable in the form factor equation. This approach, although originating in a different domain, is well-suited for the present application as it accounts for low l/d (or equivalently L/B) values characteristic of the fishing vessel.

Our analysis indicates that the $1 + k$ value for the KCS closely follows the Hoerner's curve (Hoerner, 1965), which was originally developed for configurations with high l/d ratios. In contrast, the fishing vessel demonstrates a stronger correlation with the modified Raymer's curve (Raymer, 2019), which was specifically adjusted to represent lower fineness ratio bodies more accurately.

The study concludes by examining the implications of the substantial variation in $1 + k$ with Rn on the total resistance and effective power predicted for the fishing vessel. It is proposed to implement an extrapolation methodology that incorporates distinct k values for the model and the full-scale vessel, in contrast to the conventional approach that assumes a constant k. The differences in performance prediction between this two-form-factor method and the traditional ITTC-1957 method are significant and warrant validation through comparison with sea trial data.

To strengthen the conclusions presented in this study, future research should include further experimental and numerical investigations involving model-scale vessels with low L/B ratios, supported by full-scale sea trial measurements.

Finally, it should be noted that all of the findings mentioned above directly address the four key questions raised in the introduction.

First, on the correctness of the CFD double-body (DB) implementation, by validating our DB model against the KCS benchmark and published results, we confirm that the implementation is correct; thus, the dependence of $1 + k$ observed in the fishing vessel is not a numerical artifact but a genuine hydrodynamic feature.

Second, on whether the dependence is driven by Fn or Rn, our cross-scale DB computations and model tests indicate that the variability of $1 + k$ is primarily governed by Rn, while the influence of Fn on $1 + k$ becomes negligible at moderate/high Fn. Thus, the scale (viscous) effect dominates the trend.

Third, on whether this behavior is vessel-type specific, the contrast between the fishing vessel and the KCS demonstrates that the strong, non-asymptotic increase of $1 + k$ with Rn is a distinctive feature of low L/B hulls. For the KCS, $1 + k$ stabilizes at lower Rn values, while the fishing vessel retains a higher terminal level.

Fourth, on the extrapolation strategy and the value of k to adopt, for low L/B vessels our results support the adoption of distinct form-factor values at model and full scale, instead of assuming a single constant k.

CRediT authorship contribution statement

S. Oyuela: Methodology, Investigation, Formal analysis, Data curation; **H. R. Díaz-Ojeda:** Writing – review & editing, Writing – original draft, Investigation; **A. D. Otero:** Writing – review & editing, Investigation; **R. Sosa:** Writing – original draft, Supervision, Project administration, Investigation, Conceptualization.

Declaration of competing interest

The authors declare that they have no known competing financial interests or personal relationships that could have appeared to influence the work reported in this paper.

References

American Society of Mechanical Engineers, 2009. Standard for Verification and Validation in Computational Fluid Dynamics and Heat Transfer: An American National Standard. American Society of Mechanical Engineers.

Comittee, t. I.R., 2017. ITTC, 2017. Uncertainty analysis in cfd verification and validation, methodology and procedures. ITTC - Quality System Manual Recommended Procedures and Guidelines 7, 5-03-01-01. ITTC.

Committee, t. I.P., 2017. ITTC - Recommended Procedures and Guidelines - 1978 ITTC Performance Prediction Method. ITTC.

Committee, t. I.R., 2011. ITTC - Recommended Procedures and Guidelines - Resistance Test. ITTC.

Committee, t. I.R., 2021. ITTC - The Specialist Committee on CFD and EFD Combined Methods Final Report and Recommendations. ITTC.

Conn, J.F.C., Ferguson, A.M., 1968. Results obtained with a series of geometrically similar models. Trans. Royal Institution Naval Architects 110, 255–300.

Couser, P.R., Molland, A.F., Armstrong, N.A., Utama, I.K.A.P., 1997. Calm water powering prediction for high speed catamarans. In: Proceedings of 4th International Conference on Fast Sea Transportation, FAST'97. Sydney.

Freitas, C.J., 2020. Standards and methods for verification, validation, and uncertainty assessments in modeling and simulation. J. Verif. Validation Uncertainty Quantif. 5 (2), 021001. https://doi.org/10.1115/1.4047274

García-Gómez, A., 2000. On the form factor scale effect. Ocean Eng. 27 (1), 97–109. https://doi.org/10.1016/S0029-8018(98)00042-0

Grigson, C.W.B., 2000. A planar friction algorithm and its use in analysing hull resistance. Trans. Royal Inst. Naval Architects 142, 76–115.

Group, t. I. Q.S., 2017. ITTC - General Guidelines for Uncertainty Analisys in Resistance Tests. ITTC.

Hoerner, S.F., 1965. Fluid-Dynamic Drag: Practical Information on Aerodynamic Drag and Hydrodynamic Resistance. Published by the Author, Bakersfield, CA.

Hughes, G., 1954. Friction and form resistance in turbulent flow, and a proposed formulation for use in model and ship correlation. National Physical Laboratory, NPL, Ship Division, Presented at the Institution of Naval Architects, Paper No. 7, London, April, RINA Transactions 1954-16 .

Korkmaz, K.B., Werner, S., Bensow, R., 2022. Scaling of wetted-transom resistance for improved full-scale ship performance predictions. Ocean Eng. 266, 112590. https://doi.org/10.1016/j.oceaneng.2022.112590

Korkmaz, K.B., Werner, S., Bensow, R.E., 2019. Numerical friction lines for CFD based form factor determination method. https://api.semanticscholar.org/CorpusID:166226119.

Korkmaz, K.B., Werner, S., Sakamoto, N., Queutey, P., Deng, G., Yuling, G., Guoxiang, D., Maki, K., Ye, H., Akinturk, A., Sayeed, T., Hino, T., Zhao, F., Tezdogan, T., Demirel, Y.K., Bensow, R., 2021. CFD based form factor determination method. Ocean Eng. 220, 108451.

Larsson, L., Raven, H.C., Paulling, J.R., 2010. Ship Resistance and Flow. Principles of naval architecture, Society of Naval Architects and Marine Engineers.

Larsson, L., Stern, F., Visonneau, M., 2013. Numerical Ship Hydrodynamics: An assessment of the Gothenburg 2010 Workshop. SpringerLink : Bücher, Springer Netherlands.

Molland, A.F., Turnock, S.R., Hudson, D.A., 2017. Ship Resistance and Propulsion: Practical Estimation of Ship Propulsive Power. Cambridge University Press, Cambridge. 2 edition.

OpenFOAM community, n.d. User guide: klowrewallfunction. https://www.openfoam.com/documentation/guides/latest/doc/guide-bcs-wall-turbulence-kLowReWallFunction.html.

Oyuela, S., Ojeda, H. R.D., Arribas, F.P., Otero, A.D., Sosa, R., 2024. Investigating fishing vessel hydrodynamics by using EFD and CFD tools, with focus on total ship resistance and its components. J. Mar. Sci. Eng. 12 (4). https://doi.org/10.3390/jmse12040622

Pena, B., Huang, L., 2021. A review on the turbulence modelling strategy for ship hydrodynamic simulations. Ocean Eng. 241, 110082. https://doi.org/10.1016/j.oceaneng.2021.110082

Prohaska, C.W., 1966. A simple method for evaluation of the form factor and low speed wave resistance. Proc. of 11th ITTC , 65–66.

Raven, H.C., 2016. A new correction procedure for shallow-water effects in ship speed trials. In: 13th International Symposium on Practical Design of Ships (PRADS 2016). Copenhagen, Denmark. MARIN report.

Raymer, D.P., 2019. Aircraft Design: A Conceptual Approach. AIAA Education Series, AIAA, Reston, VA. 6 edition.

Specialist Committee: Procedures for Resistance, P., Propeller Open Water Tests of 23rd ITTC, 2002. ITTC - Recommended Procedures and Guidelines: Model Manufacture, Ship Models. ITTC.

Roskam, J., 1987. Airplane Design. Roskam Aviation and Engineering Corp., Ottawa, KS.

Shevell, R.S., 1989. Fundamentals of Flight. Prentice-Hall, Upper Saddle River, NJ. 2 edition.

Song, S., Demirel, Y., Atlar, M., Dai, S., Turan, O., 2019. Validation of the CFD approach for modelling roughness effect on ship resistance.

Terziev, M., Tezdogan, T., Demirel, Y.K., Villa, D., Mizzi, S., Incecik, A., 2020. Data for: "exploring the effects of speed and scale on a ship's form factor using CFD". https://doi.org/10.15129/177ff072-cd23-4762-9492-2f495a4879d3

Terziev, M., Tezdogan, T., Demirel, Y.K., Villa, D., Mizzi, S., Incecik, A., 2021. Exploring the effects of speed and scale on a ship's form factor using CFD. Int. J. Naval Architecture Ocean Eng. 13, 147–162. https://doi.org/10.1016/j.ijnaoe.2020.12.002

Terziev, M., Tezdogan, T., Incecik, A., 2019. A geosim analysis of ship resistance decomposition and scale effects with the aid of CFD. Appl. Ocean Res. 92, 101930. https://doi.org/10.1016/j.apor.2019.101930

Terziev, M., Tezdogan, T., Incecik, A., 2022. Scale effects and full-scale ship hydrodynamics: A review. Ocean Eng. 245, 110496. https://doi.org/10.1016/j.oceaneng.2021.110496

Torenbeek, E., 2010. Synthesis of Subsonic Airplane Design: An Introduction to the Preliminary Design of Subsonic General Aviation and Transport Aircraft, with Emphasis on Layout, Aerodynamic Design, Propulsion and Performance. Springer, Dordrecht, The Netherlands.

WANG, Z.-z., XIONG, Y., SHI, L.-p., LIU, Z.-h., 2015. A numerical flat plate friction line and its application. J. Hydrodyn. Ser. B 27 (3), 383–393. https://doi.org/10.1016/S1001-6058(15)60496-6

Wright, B.D.W., 1984. Apparent viscous levels of resistance of a series of model geosims. Technical Report WG/H99. BSRA.

Yokoo, K., 1960. Effect of sinkage and trim on form factor of resistance. J. Zosen Kiokai 1960 (108), 15–22. https://doi.org/10.2534/jjasnaoe1952.1960.108_15

York, D., Evensen, N., Ló, M., Nez, M., De, J., Delgado, B., 2004. Unified equations for the slope, intercept, and standard errors of the best straight line. Am. J. Phys. - AMER J PHYS 72. https://doi.org/10.1119/1.1632486

Yılmaz, H., Kükner, A., 1999. Evaluation of cross curves of fishing vessels at the preliminary design stage. Ocean Eng. 26 (10), 979–990. https://doi.org/10.1016/S0029-8018(98)00038-9

Zeng, Q., Hekkenberg, R., Thill, C., 2019. On the viscous resistance of ships sailing in shallow water. Ocean Eng. 190, 106434. https://doi.org/10.1016/j.oceaneng.2019.106434